WILEY | Hindawi

Research Article

Experimental Study on Compression and Torsion Fracture within 3D Printed Cementation-Weak and Porosity-High Sandstones

Xiaodong Zhao [ID],[1] Xu Cai,[1] Xingya Zhou,[1] Zejin Lai,[2] Qingwen Zhong,[1] Zhaoxiang Chu,[1] Guoqing Zhou,[1] and Hong Li[3]

[1]*State Key Laboratory for Geomechanics and Deep Underground Engineering, China University of Mining and Technology, Xuzhou, Jiangsu 221116, China*
[2]*Gannan University of Science and Technology, Ganzhou, Jiangxi 341000, China*
[3]*China Construction Tunnel Corp., Ltd, Chongqing 401320, China*

Correspondence should be addressed to Xiaodong Zhao; zxdcumt@126.com

Cretaceous sandstones have weak cementation and high porosity while exhibit a high apparent brittleness. Compression and torsion (C-T) fractures are widely distributed in Cretaceous sandstones due to asymmetric tectonic convergence action. However, studies on C-T fracture formation and the mechanisms causing variability in Cretaceous sandstones containing no oil or gas are rare due to the challenges in sampling intact sandstone cores, despite their significance to mine shaft sinking. Therefore, this study used binder jetting-based 3D printing to prepare artificial Cretaceous sandstone and developed a real-time X-ray computed tomography- (CT-) aided torsion shear apparatus to test them. The test results showed that the 3D printed (3DP) sandstone had characteristic indexes that approached and even exceeded the lower limits of Cretaceous sandstone cores, thereby accurately representing the unavailable cores. Furthermore, the 3DP sandstones had anisotropic properties comparable to the sandstone cores. Under C-T action, the 3DP sandstone exhibited a pronounced strain gradient of 2.0 %/mm perpendicular to fracture inclination. The inclination angles of fractures formed under C-T action tended to increase as the cell pressure increased, and that approached the orientation angles of maximal principal stress. The maximal and minimal principal stresses exerted inclination-slip and width-stretching effects, respectively, on C-T fractures. But the effect of inclination-slip on the C-T fractures was stronger than that of width-stretching. This insight into C-T fracture formation will guide future studies on the fracture evolution and its disaster-dominating mechanisms arisen from disturbances by shaft sinking.

1. Introduction

There are over 300 coal-bearing basins in China according to the definitions given by the China National Coal Association. Among these, Ordos, Junggar, Tarim, Turpan-Hami, and Sichuan basins are located in Western China. Western China has been the primary region for coal resource exploration and utilization for the next decades, helping to meet the massive energy demands of China [1].

As can be seen in Figure 1, the coal in Western China was mostly concentrated in Jurassic stratum with a portion of that extending into the Permian stratum in Szechwan basin. As part of the coal mining process, shafts are extensively used for the upwards transportation of coal, downwards transportation of personnel, materials, and ventilation [2–4], they are choke-points of mines. Unlike inclined shafts and roadways, shafts often cross various geological formations, including Cretaceous sandstone overlying Jurassic stratum which has poor cementation and high porosity [5–8]. Due to these cementation-poor and porosity-high characteristics, the Cretaceous sandstones are highly susceptible to shaft sinking. Disturbed by the shaft sinking, the cementation between grain matrixes can be broken, which further increased the porosity of sandstones. This might result in an inrush of underground water along with
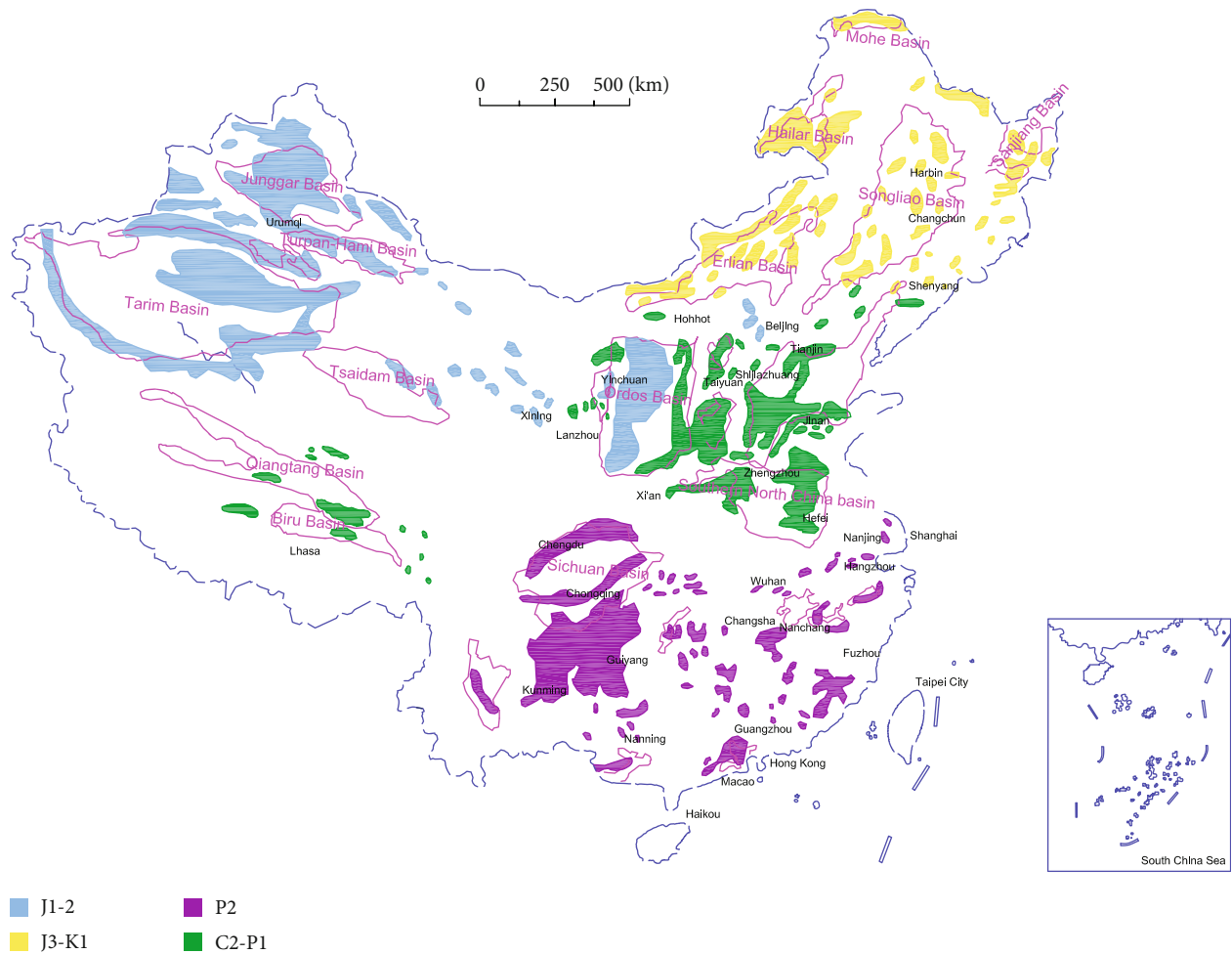
Figure 1: Coal-bearing basins in China.

the delaminated fine grains during shaft sinking. The inrush of water and fine grain mixtures can cause leakage and even rupture shaft linings [5, 9]. Therefore, numerous studies have been performed to investigate the coupled hydromechanical properties of weakly cemented sandstones [6, 10, 11]. It has been well recognized that the weakly cemented sandstones cannot be identified as rock-like or soil-like geomaterials [8, 12, 13].

Meanwhile, as observed in previous tests, weakly cemented sandstone exhibits brittle characteristics despite its high porosity [10, 11, 14]. According to the obtained publications in the petroleum geology field, the terrains of these coal-bearing basins are generally flat with almost no faults or folds growing within them. However, there are tectonic fractures that are distinguished from the diagenetic and natural fractures widely distributed within these coal-bearing basins, and this phenomenon is more remarkable near the orogen-basin transition zone [15–21]. The formation of tectonic fractures has been associated with convergence actions close to or even far away from strike-slip faults and transpressional structures [18, 22]. In other words, where there was structural convergence, there was compression and torsion (C-T) action because convergence is usually asymmetric [23, 24]. In particular, convergence-induced compression stress is usually attenuated as it propagates from orogen to basin [20].

The mechanisms governing tectonic fractures due to C-T action are similar to those governing C-T faults, but are carried out over relatively small scales [16]. Tectonic fracture can greatly affect oil/gas production by altering the seepage characteristics of sandstone reservoirs. This made it a primary focus of oil/gas geological research. However, the tectonic fractures developed within Cretaceous sandstones containing no oil/gas have attracted relatively little attention, despite their importance on shaft sinking [1, 25]. This may be because it is especially difficult to accurately detect the tectonic fractures during geotechnical explorations due to their small scales. Furthermore, whether small-scale boreholes or the relatively large-scaled shafts encountered the C-T fractures cannot be accurately predicted due to the random distribution of C-T fractures in space. In fact, the extension of C-T fractures have been showed to be on the same order of magnitude as shaft diameters, which greatly enhances the interaction between shafts and surrounding rocks.

Recognizing the shaft sinking-related disturbances to C-T fracture variations is crucial to developing a reasonable shaft sinking method and evaluating the long-term serving performances of shaft lining. A precondition for achieving this aim is to understand the fracture formation process and the corresponding stress rotation.

Indoor experimental study is an invaluable method for investigating the deformation and strength behaviors of geomaterials under C-T actions [26]. Compared with true triaxial compression apparatus, the principal stress level and its orientation under complex stress paths can be achieved comprehensively by controlling the axial load, torque, and inner and outer cell pressures independently using a torsional shear apparatus to replicate C-T action. Early torsional shear apparatuses were mainly used in the study of soft soils [27], but were later extended to frozen soils [28] and rocks [29, 30], with the aim of developing strength criteria under complex stress states. But the aforementioned methods do not allow the visualization of specimens, which has limited our understanding of the microcosmic mechanisms therein. In order to make up such deficiency, traditional X-ray CT, synchrotron X-ray micro CT, and even electronuclear machine-CT have been successively incorporated into triaxial tests with observational accuracies ranging from mm to μm scale [31, 32]. The study used in-situ CT aided torsional shear tests for the visualization of C-T fractures, which has not previously been attempted despite its potential to significantly enhance our understanding of fracture formation process and the disaster-dominating mechanisms that originate from fracture evolution.

In this present study, a real-time X-ray CT aided torsional shear apparatus was developed. Then, a 3D printing method was used to prepare cementation-weak and porosity-high sandstones to model the unavailable Cretaceous sandstone cores. The fracture characteristics within the 3D printed (3DP) sandstones under typical C-T paths were investigated. The significances of this study to recognize the tectonic fracture formation and reveal its influences on shaft sinking were discussed.

2. Test Methodology

2.1. Real-Time X-Ray CT-Aided C-T Apparatus. According to a previous study utilizing the torsional shear apparatus and hollow cylinder tests [33], a real-time X-ray CT-aided C-T apparatus capable of performing experiments on tectonic fracture formation and its variation induced by artificial freeze-thaw during shaft sinking and grouting during shaft lining maintenance was developed as shown in Figure 2. The real-time X-ray CT-aided C-T apparatus consisted of a CT scanner, a C-T controller, two cell pressure controllers, a test chamber, and a data acquisition instrument. The CT scanner could have been medical or industrial depending on the required scanning accuracy in test. The C-T controller included an axial stress device and a torque loading device. The test chamber and four stand columns within the scanning range were manufactured out of 7075 aluminum alloy allowing high X-ray transmissivity [34]. The upper and lower plates were integrated with the four stand columns to resist the torsion action. In the interest of portability, so that the apparatus could be better compatible to various CT scanners, the height of the test apparatus was set to 1.0 m with a maximum lateral width of 0.4 m.

The axial, inner, and outer cell pressures were powered by separate stepping motors. The torsion was powered by a turbine worm gear device. The automatic control was fundamentally similar to that described in the publication by Zhao et al. [35]. The newly-developed apparatus was primarily designed for cementation-weak and porosity-high sandstones with relatively low compressive strength. Accordingly, the maximal axial load, torque, and cell pressure were set to 30 ± 0.15 KN, 300 ± 1.5 N·m, and 5 ± 0.001 MPa, respectively.

The test procedure was slightly different from the previously reported torsional shear apparatus [27, 28]. The C-T controller was installed separately after the completion of the hollow cylindrical specimen, inner membrane, outer membrane, and test chamber. The test action was enabled by four bulges on both the top cap and pedestal designed to achieve the torque transmission from the torsion controller to the specimens.

2.2. 3DP Sandstone Preparation. As previously mentioned, it is challenging to obtain intact Cretaceous sandstone cores with quantitative anisotropy, which hindered the accurate reproduction of the unique behaviors occurring at shaft sinking sites. Therefore, 3D printing-based artificial reconstitution of the Cretaceous sandstones in the lab was used as an alternative to avoid such limitations. The existing 3D printing methods can be divided into fused deposition modeling, stereo lithography apparatus, selective laser sintering, and binder jetting. They can be implemented in the preparation of various products with metal, plastic, and photopolymer substances. Binder jetting-based 3D printing was initially developed for casting molds and has been successfully incorporated into geomechanical test because the silica sand that it uses is the main component of sandstone. [36–39] In this study, a binder jetting-based 3D printing method was used to prepare cementation-weak and porosity-high sandstones. As shown in Table 1, sand with grain sizes ranging from 0.075 mm to 0.3 mm and with silica content over 99.5% was used as the matrix grains of the sandstones. Furan resin was used as the cementing agent to cement the silica grains. The layer thickness was set to 0.3 mm in printing. The hollow cylindrical sandstones here were slightly different than those used previously because of the focus of this study on replicating fracture evolution [28]. Based on a study of frozen saturated sand by Zhao et al. [33] and the available space of newly-developed test apparatus, an inner radius of 20 mm, an outer radius of 50 mm, and a height of 100 mm were therefore ultimately chosen for 3DP sandstone dimensions.

3. Comparisons between Sandstone Cores and 3DP Sandstones

3.1. Physical and Mechanical Properties. As shown in Figure 3, sandstone cores were gathered from nine typical shaft sinking sites situated in south central and north-central Ordos basin. The maximum thickness of the Cretaceous in the western zones of Ordos basin approached 1300 m while the thickness in the eastern Ordos basin was less than 600 m [40].

The thin section observation of Cretaceous sandstone core from HLS was performed and the results are shown in Figure 4, where the sampling depth was 274 m. The primary grains of the core were quartz with irregular shapes and feldspar with rectangular shapes. Clay minerals with maroon coloration were adsorbed on the surface of the matrix grains. The pores were characterized as having pink coloration and
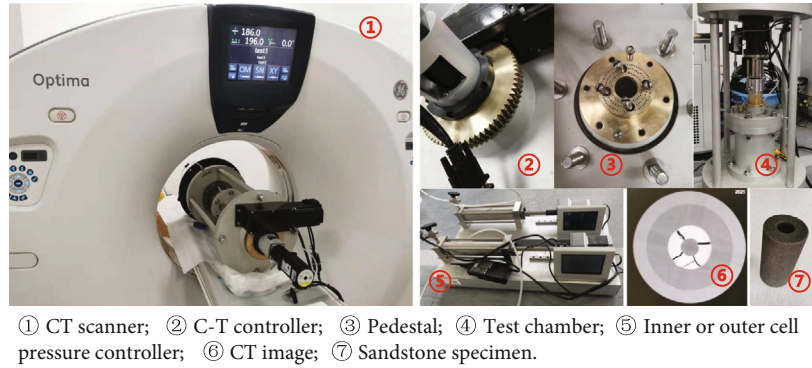
① CT scanner; ② C-T controller; ③ Pedestal; ④ Test chamber; ⑤ Inner or outer cell pressure controller; ⑥ CT image; ⑦ Sandstone specimen.

FIGURE 2: Real-time X-ray CT-aided C-T test apparatus.

TABLE 1: Grain size composition.

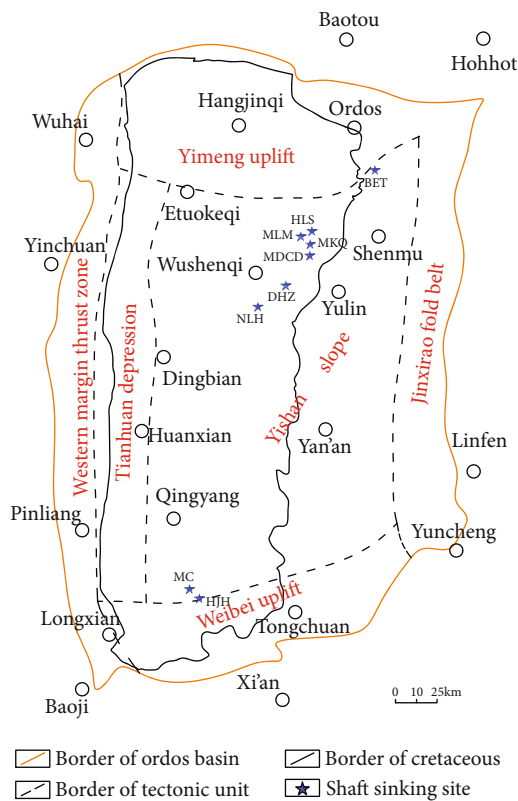| Grain size/mm	0.212~0.3	0.15~0.212	0.106~0.15	0.075~0.106	0.053~0.075
Percentage/%	30.45	62.61	8.8	0.05	0

FIGURE 3: Shaft sinking sites in Ordos basin after Hou et al. [40].

being relatively loose. The remaining grains had subangular shapes and filled in the pores formed by quartz and feldspar. The cementation in the Cretaceous sandstone was mainly from the cementation from dehydration of clay minerals to matrix grains and the slight inlay or occlusion between matrix grains. Therefore, the Cretaceous sandstones exhibited noticeable cementation-weak and porosity-high characteristics. However,

a portion of the feldspar grains were corroded leading to pores within grains despite diagenesis being relatively weak within the sandstones.

Figure 5 provides a 2D CT image of the 3DP sandstone. The quartz grains were irregular with sharp corners because they had not experienced any abrasion from natural processes that occur during sedimentation. Some grains were cemented by the furan resin with line-line and point-line contacts. Figure 6 shows the typical uniaxial stress-strain response of Cretaceous sandstone cores from BET and HLS in the Ordos basin and 3DP sandstones, where sandstone cores A1, A2, and A3 were from BET [41]. The sampling depths of these sandstone cores ranged from 85.8 to 88.8 m. The loading rate was 0.3 mm/min. Specimens C1and C2 were 3DP sandstones with a cementing agent content of 80% and a loading rate of 0.2 mm/min. The loading rate of the sandstone core from HLS was 0.2 mm/min. The diameters and heights of all sandstone specimens in Figure 6 were 50 mm and 100 mm, respectively. Figure 6 shows that the stress-strain curve of the two types of sandstones. From Figure 6, the 3DP sandstones exhibited a brittle behavior identical with sandstone cores. It was thus practicable to reproduce the fracture observed in field within 3DP sandstones. However, due to the remarkable randomness in physical and mechanical properties of Cretaceous sandstone cores independent of sampling depth, a specific statistical analysis was necessary to process the physical and mechanical indexes of Cretaceous sandstone cores for quantitative interpretation of the comparability with the sandstone cores. It should be noted that the lower limits of density, tensile/compressive strength, elastic modulus, internal friction angle and cohesion corresponded to an upper limit of Poisson's ratio and porosity according to the statistical data that were used to represent the unavailable sandstone cores. In other words, the obtained data in Figure 6 for intact sandstone cores cannot comprehensively reflect the Cretaceous sandstones with cementation-weak and porosity-high characteristics.

Table 2 lists the upper and lower limits of the physical and mechanical indexes of the Cretaceous sandstone cores.
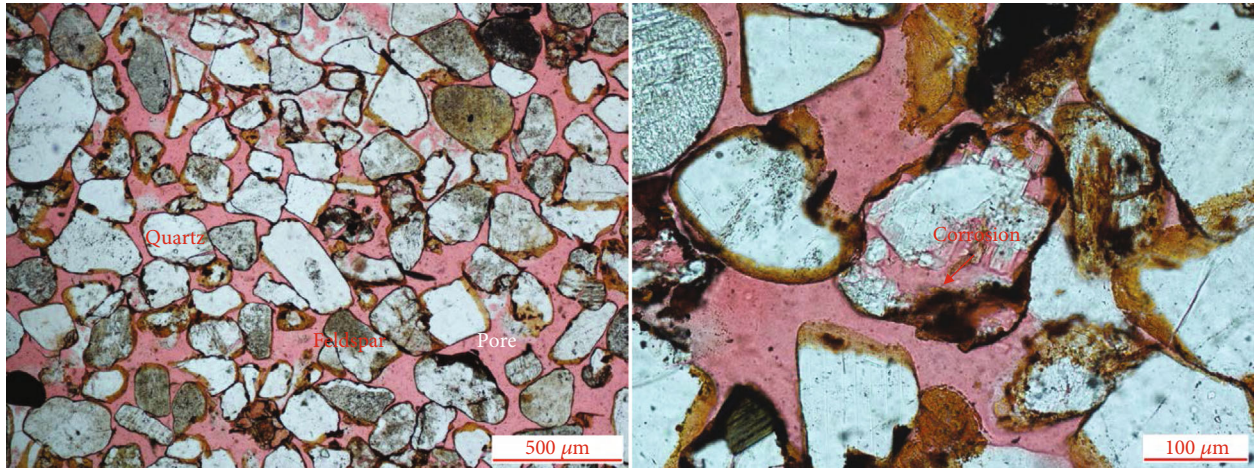
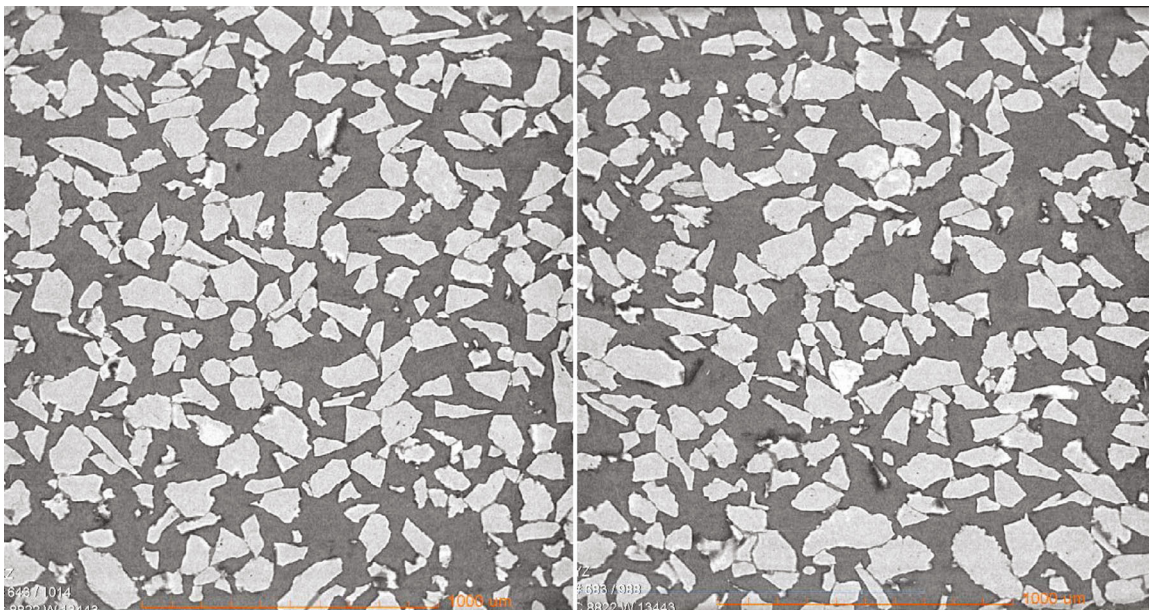FIGURE 4: Thin sections of sandstone cores from HLS.

FIGURE 5: 2D CT image of 3DP sandstone.

The sample data from BET cores were gathered from Li et al. [42] and the remaining sample data were from geotechnical survey reports organized by the China Coal Xi'an and Handan Design Engineering Co., LTDs. Table 2 provides the porosity n of sandstone cores determined as the ratio between the volume of water intake and specimen volume, the compressive strength σ_c determined as the peak stress observed in the uniaxial compression test, the elastic modulus E and Poisson's ratio μ from the slope of the linear stage of the stress-strain and lateral strain-axial strain curves, respectively, $\tan \varphi$ and cohesion c in triaxial compression tests determined from the slope and intercept of tangent of Mohr circles under various confining pressures, respectively, and the tensile strength σ_t was determined as the peak stress in Brazilian splitting test of Cretaceous sandstone cores from various shaft sinking sites situated in Ordos basin. The loading rates in compression tests

and Brazilian splitting tests were identical. Further, the formula $\sigma_c' \bullet \sigma_t'/2$ proposed by Altindag [43] was employed to quantitatively assess the brittleness of the sandstone cores. Where σ_c' and σ_t' are dimensionless σ_c and σ_t.

From Table 2, the Cretaceous sandstone cores in the southern Ordos basin were stronger than those in the northern Ordos basin with a porosity being lower than that in the northern Ordos basin. This might be related to the differences in clay mineral content. However, there was a small amount of variability in the internal friction angle which reflected the slight variations in the main substances within the Cretaceous sandstone cores.

The ranges of upper limits of porosity n and Poisson's ratio μ as well as the lower limits of density, compressive strength σ_c, tensile strength σ_t, elastic modulus E, internal friction angle φ, and cohesion c of the Cretaceous sandstone
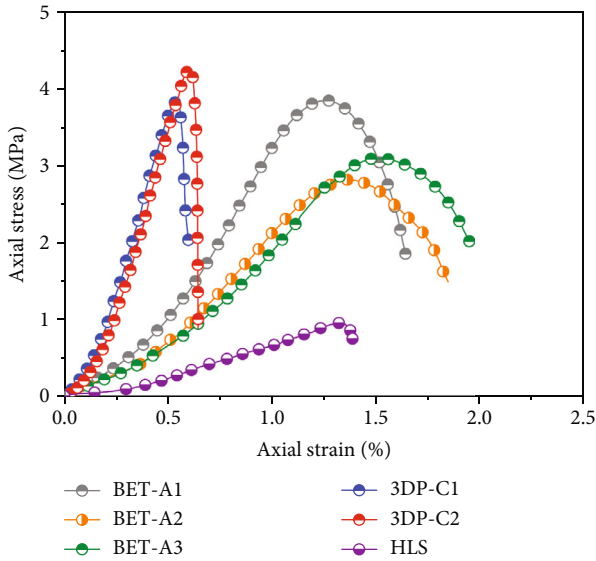
FIGURE 6: Stress-strain curves of 3DP sandstones and sandstone cores.

cores are listed in Table 3. The densities of 3DP sandstones were lower than those of Cretaceous sandstone cores, while the porosities of the 3DP sandstones were higher than those of the Cretaceous sandstone cores. The cohesion values and internal friction angles were greater in the 3DP sandstones than in the Cretaceous sandstone cores. The remaining indexes fell into a range limited by the sample data from different shaft sinking sites.

The underlying reasons for the differences between cores and 3DP sandstones were due to differences in cementing agent characteristics and the corresponding cementation strength. The solidified cementing agent was more brittle and had a stronger cementation effect on grains in 3DP sandstones compared to the dehydrated clay minerals in the Cretaceous sandstones. Further, the furan resin just provided cementation at limited contact points and the occlusion effects occurred between grain corners. These combined reasons caused the observed strength of the 3DP sandstones to approach the strength of the sandstone cores despite the lower specimen density. Meanwhile, the addition of cementing agent altered the substance composition sandstones, thus affecting the friction behaviors among particles along with friction angle and cohesion. Despite the differences, the main physical and mechanical indexes of the 3DP sandstones were comparable to the cores, indicating the 3DP sandstones can represent and model the unavailable Cretaceous sandstone cores.

3.2. Anisotropic Behaviors. The tectonic fracture formation in Cretaceous sandstone is strongly dependent on the anisotropic properties of the sandstone reservoir. But the properties of sandstone cores can appear random because they are easily altered by sampling due to their weak cementation and high porosity. The obtained sandstone cores were thus not the problematic sandstones and therefore not suitable to be used to quantitatively investigate how heterogeneity influences the C-T fractures. In order to investigate how the specimen-scaled anisotropic properties of the 3DP sandstone influenced

C-T fracture formation, the particle-scaled anisotropy should be addressed firstly. A concept of equivalent ellipse was initially proposed to give an approximate description of grains. The shape factor r_p was expressed as a ratio between major and minor axes of the equivalent ellipse. Figure 7 shows the shape factor r_p of grains used in 3DP sandstones. The shape factors of the 3DP grains ranged from 1.1 to 4.1, with a mean value of 2.6 and a variance of 0.85. Further, the shape factors of most grains were less than 2.5. Clearly, the shapes of grains were not standard circles, which inevitably influenced the specimen-scaled anisotropic properties of the 3DP sandstone.

Figure 8 shows the acute angle α between the major axes of equivalent ellipses and the vertical plane in the transection and horizontal plane in the orthotropic longisection, where the angles between major axes of equivalent ellipses and the positive axes ranged from 0° to 90°, and from 0° to -90° between major axes of equivalent ellipses and the negative axes. As indicated in Section 2.2, the grain packing direction was perpendicular to the horizontal plane. Based on Figure 8, the proportion of grains with different α values in the transection fluctuated between 4.3% and 6.8% with an average value of 5.6%, which indicated a relatively uniform distribution. However, there was a remarkable nonuniformity in the proportion of grains with different α values in the orthotropic longisection. Although the largest proportion of grains of 11.6% was found to be concentrated on the range of $-30\circ \leq \alpha \leq -20\circ$, the distribution of the major axes of the remaining grains showed a slight preference for the horizontal plane with approximately 50% concentrated in the range of $-30\circ \leq \alpha \leq 30\circ$ due to the paving and smoothing processes during 3D printing. The right tail probability calculated via chi-square test was 23% > 5%. The distribution of major axes orientations thus accorded with a normal distribution. Therefore, the grain skeleton structures in the transection and longisection were different. In other words, the 3DP sandstone had isotropic properties within the transection and anisotropic properties in the transection and longisection. According to the previous studies [44, 45], sandstone formed during a natural sedimentation exhibits an obvious anisotropic strength behavior. The strength is usually reduced due to a decrease in the angle between stratification and loading direction with a maximal strength occurring along the vertical direction.

4. Digital Image Correlation-Based C-T Fracture Characterization

To validate the reliability of the test results from the real-time X-ray CT-aided C-T apparatus, a uniaxial C-T test was performed with the aid of digital image correlation (DIC) analysis. The displacement observation precision of the DIC was ±0.001 pixels, which corresponded to a strain identification precision of ±10 $\mu\varepsilon$. The loading rate of the axial piston was 0.2 mm/min with a torque loading rate being 2°/min in the test. The torsion application corresponded to an axial load of 3 KN. The digital images and shear strain distributions were recorded at the initial stage, torsion application stage, peak torque stage, and 22.5 s and 39 s after the peak torque stage, as shown in Figures 9 and 10, respectively. In Figure 10, the lateral width

TABLE 2: Upper/lower limits of physical and mechanical indexes of Cretaceous sandstone cores.

Shaft sinking site(number of cores)	ρ_d (g/cm^3)	n (%)	σ_c (MPa)	σ_t (MPa)	c (MPa)	φ (°)	E (GPa)	μ	$\sigma'_c \cdot \sigma'_t/2$
HLS(40)	1.87	29.2	4.4	0.21	0.70	31.0	1.30	0.28	0.46
MDCD(24)	1.99	25.2	17.1	0.04	0.11	40.5	0.19	0.37	0.34
MLM(12)	1.93	32.2	8.3	0.83	—	—	0.38	0.23	3.44
MKQ(29)	2.29	18.1	5.6	0.20	0.38	36.2	0.33	0.30	0.56
NLH(15)	1.92	28.0	13.5	0.51	0.46	35.8	1.77	0.26	3.44
DHZ(17)	1.89	29.2	4.9	0.04	0.02	34.0	0.01	0.39	0.10
MC(29)	2.21	8.98	16.8	0.69	3.33	28.6	1.08	0.26	5.80
HJH(3)	2.42	12.9	20.5	—	1.24	38.5	—	0.29	
BET(14)	1.94	27.5	4.1	0.10	4.80	29.2	0.52	—	0.21

TABLE 3: Comparisons between Cretaceous sandstone cores and 3DP sandstones.

Index	3DP sandstone	Sandstone cores
ρ_d (g/cm^3)	1.23	1.87~2.42
n (%)	35.4	9.0 ~ 32.2
σ_c (MPa)	4.17	4.10~20.50
σ_t (MPa)	0.61	0.04~0.83
c (MPa)	0.80	0.02~4.80
E (GPa)	3.86	0.01~1.77
φ (°)	47.0	28.6 ~ 40.5
μ	0.4	0.23~0.39
$\sigma'_c \cdot \sigma'_t/2$	1.27	0.10~5.80
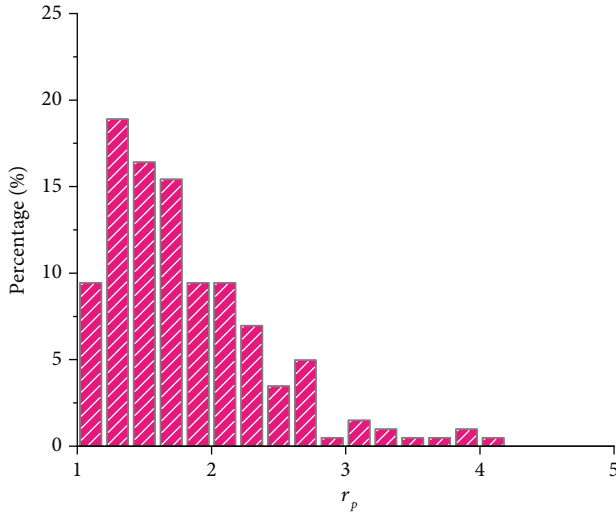
FIGURE 7: Distribution of shape factor r_p.

that was analyzed was 30 mm and the vertical height that was analyzed was 100 mm, and when there was a positive shear strain implied that the angle of strain block decreased, while a negative strain implied that the angle of the strain block increased.

As can be noted from Figures 9 and 10, the observable fracture was not formed until the torque peaked, although there were unavoidable microcracks that occurred within the 3DP sandstone. The shear strain was distributed uniformly over the specimen surface, except at some scattered locations at upper end of the specimen. However, after the peak torque, the observable fracture generated. The fracture had fully penetrated the sandstone specimen at 25 s after the peak torque with a measured expansion rate of 10.4 mm/s. From Figure 10, the length and width of fracture were 110 mm and 1.8 mm, respectively, while the width of the zone with a prominent shear strain gradient ranged from 1 mm to 4 mm with an average width of 2.75 mm.

Although numerous studies on strain localization have been conducted [46], no studies on strain gradient formed under C-T had been made available at the time of this study. In fact, the nature of strain gradient was heterogeneity in the anisotropic sandstone specimens and influenced the latter fracture formation under multiperiod tectonic actions. Figure 11 shows the strain gradients in the parallel and perpendicular directions relative to the fracture. The three blue data points represent the averaged values of five points with an interval of 25% of the fracture length at the distances from the fracture margin of 0 mm, 0.65 mm, and 1.30 mm, respectively. The red data points represent the shear strain parallel to the C-T facture with an interval of 10% fracture length. The strain gradient parallel to the C-T fracture was 8.1×10^{-3}%/mm, whereas it was 2.0%/mm perpendicular to the C-T fracture. Hence, the zone perpendicular to fracture had a pronounced strain gradient while the strain gradient in the zone along the fracture was negligible.

Based on the findings by Chen et al. [28] and Lai [44], as the torque was increased, the stress state within 3DP sandstones varied from compressive shear to torsional shear when the principal stress orientation angle was ≤45∘ and the shear strain under an identical shear stress was increased. The compressive shear induced shear strain and its gradient neighboring the C-T fracture was gradually neutralized by torsional shear. In other words, the implementation of torsion significantly changed the course of strain gradient near observable fracture as shown in Figure 10.

5. X-Ray CT-Aided C-T Fracture

5.1. Principal Stress State. Because the test chamber was not transparent, it was challenging to perform DIC analysis during
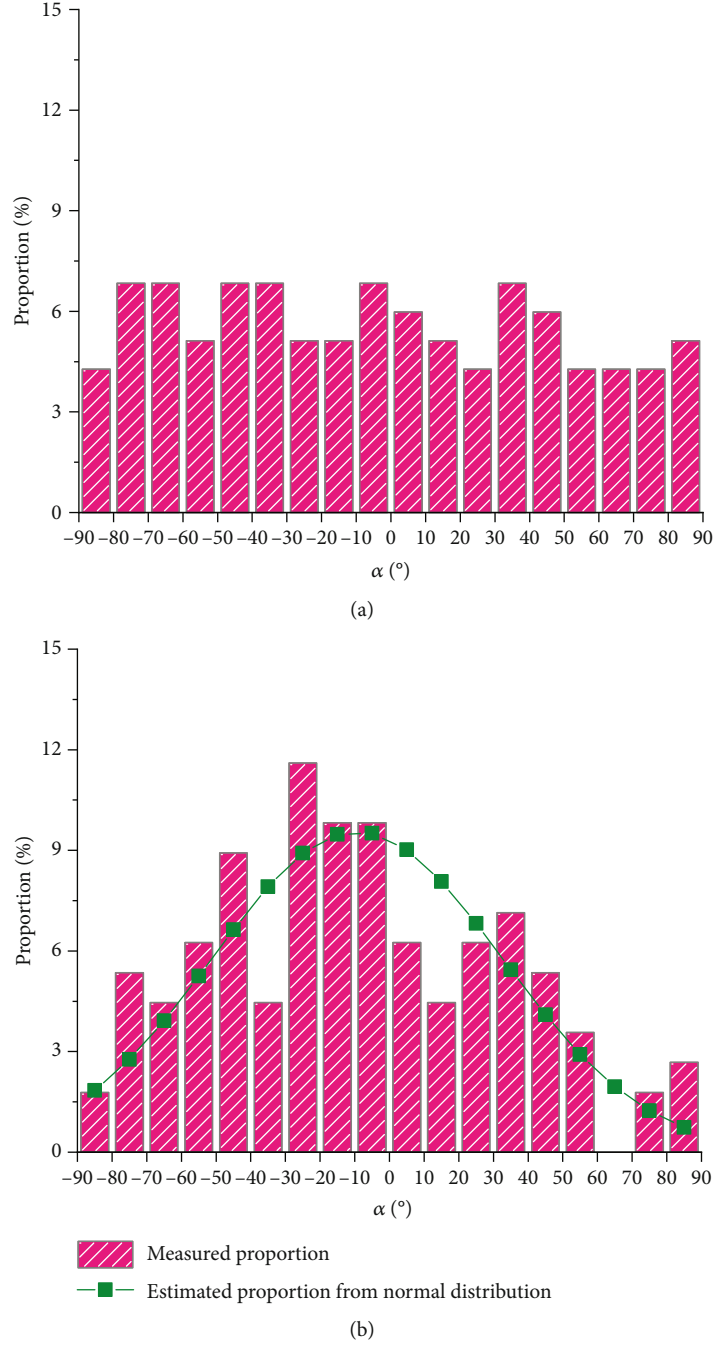
(a)

Measured proportion

■ Estimated proportion from normal distribution

(b)

FIGURE 8: Distribution of α in the (a) transection and (b) longisection.

the triaxial C-T test. Accordingly, four X-ray CT-aided C-T tests were carried out as indicated in Table 4. The 3DP sandstones were initially consolidated isotropically to reach similar inner cell, outer cell, and axial pressures. Subsequently, an axial load increment of 3 KN was applied. Afterwards, the torque varied following a rate of 2°/min until reaching and then exceeding the peak torque. Based on the observations in Section 4, the C-T fracture followed after peak torque was reached. So the CT observation points were optimized into three stages, namely, initial stage, torsion application stage, and after peak torque stage.

The axial piston was different from the pistons that have been reported in previous torsional shear apparatuses [28, 44]. The axial, radial, circumferential, and torsional shear stresses were computed as follows:

$$\sigma_z = \frac{F}{\pi\left(r_o^2 - r_i^2\right)} - \frac{p_i r_i^2}{r_o^2 - r_i^2}\,;\, \sigma_r = \frac{p_o r_o + p_i r_i}{r_o + r_i} = p_o = p_i\,;$$

$$\sigma_\theta = \frac{p_o r_o - p_i r_i}{r_o - r_i} = p_o = p_i\,;\, \tau_{z\theta} = \frac{M(r_o + r_i)}{\pi\left(r_0^4 - r_i^4\right)},$$
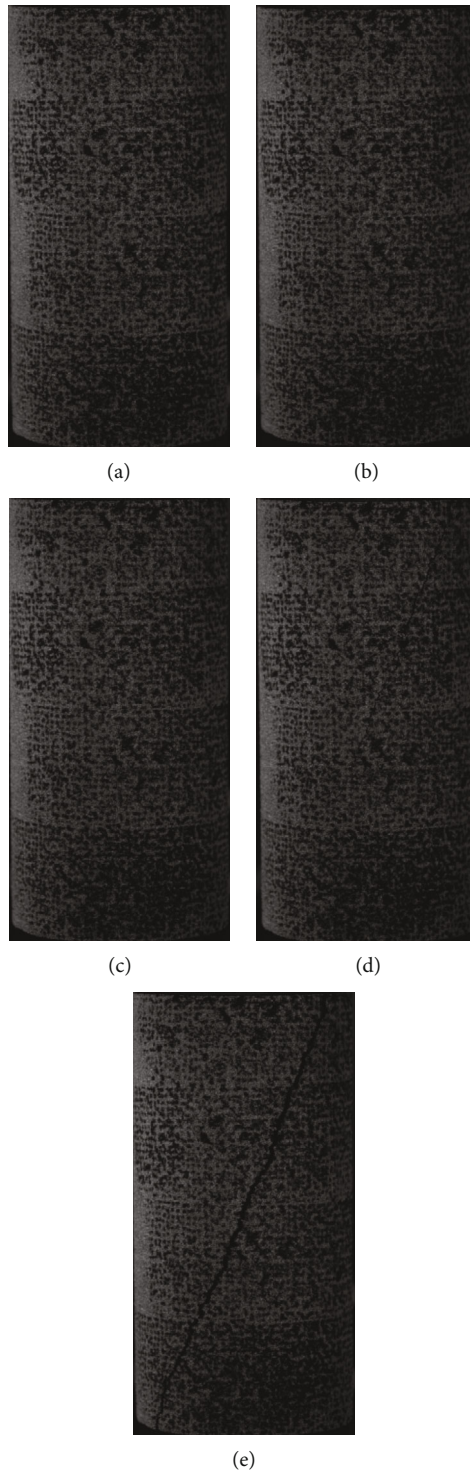
(1)

(a)

(b)

(c)

(d)

(e)

Figure 9: Digital images under (a) initial stage, (b) torsion application stage, (c) peak torsion stage, (d) 22.5 s after peak torque stage, and (e) 39 s after peak torque stage.
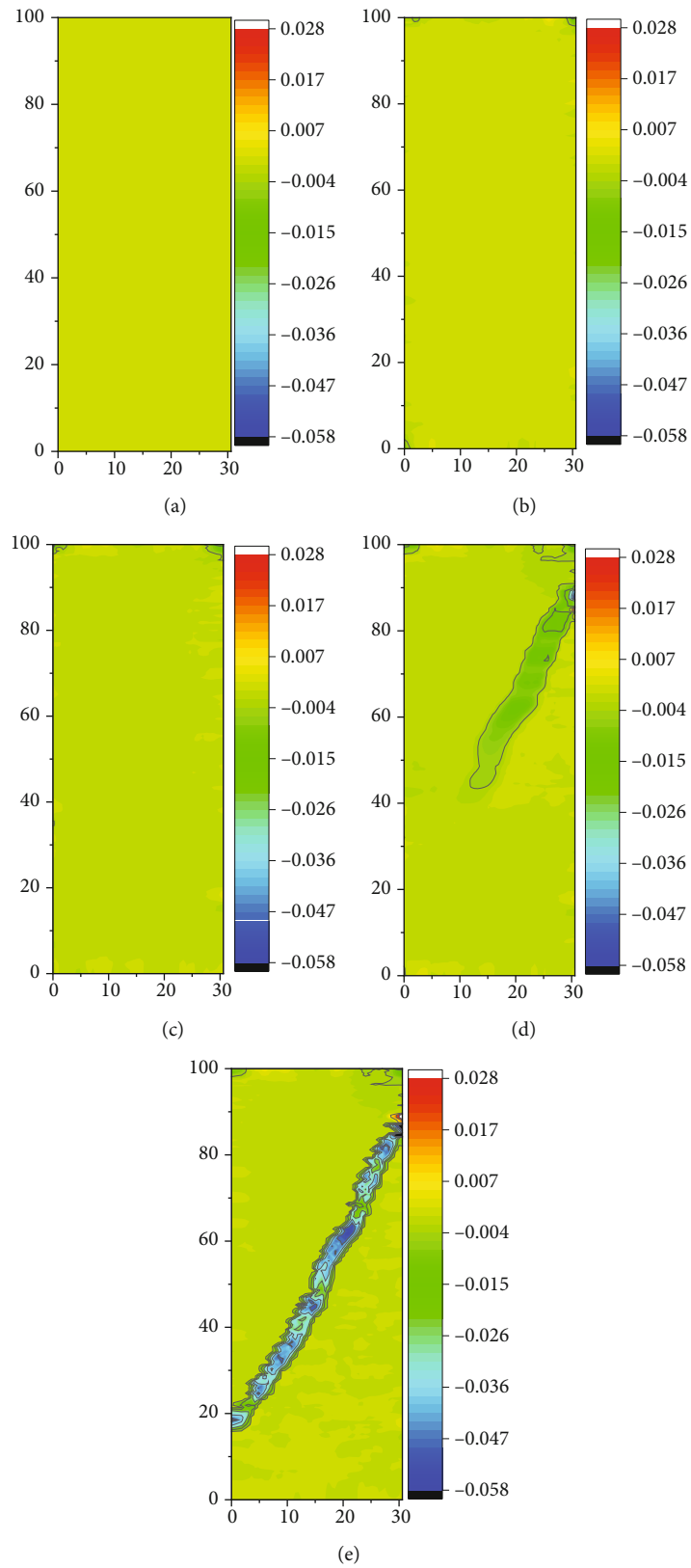
Figure 10: Shear strain distribution at (a) initial stage, (b) torsion application stage, (c) peak torque stage, (d) 22.5 s after peak torque stage, and (e) 39 s after peak torque stage.
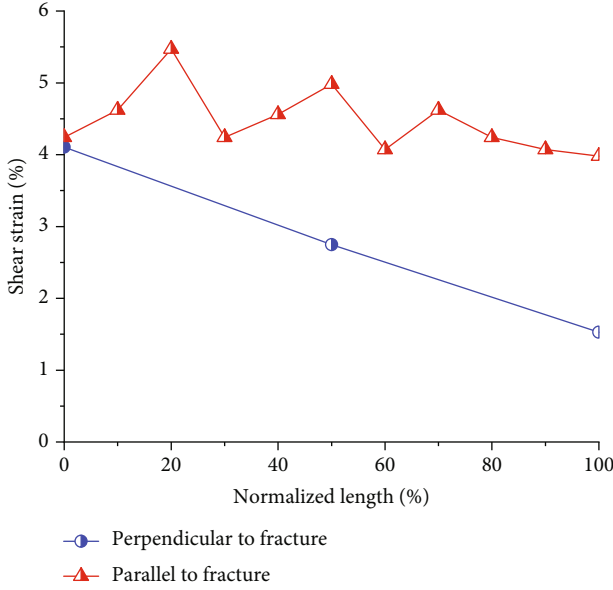
FIGURE 11: Shear strain gradient neighboring the C-T fracture.

TABLE 4: Test setup.

No	$p_o = p_i$	Axial load corresponding to torsion application	Peak torque
#1	0.00	3.0	32.4
#2	0.02	3.0	38.0
#3	0.50	3.8	65.7
#4	2.00	6.3	86.0

where F is axial load, KN; M is torque, Nm; p_o and p_i are outer and inner cell pressures, respectively, MPa; r_o and r_i are the outer and inner radiuses of specimen, respectively, mm; σ_z is the aixal stress, MPa; σ_r is radial stress, MPa; and σ_θ is circumferential stress, MPa; and $\tau_{z\theta}$ is torsion stress, MPa.

The maximal σ_1, minimal σ_3, and intermediate σ_2 principal stresses were thus obtained according to Equation (1).

$$\sigma_1 = \frac{\sigma_z + \sigma_\theta}{2} + \sqrt{\frac{(\sigma_z - \sigma_\theta)^2}{4} + (\tau_{z\theta})^2} \; ; \sigma_2 = \sigma_r \; ;$$

$$\sigma_3 = \frac{\sigma_z + \sigma_\theta}{2} - \sqrt{\frac{(\sigma_z - \sigma_\theta)^2}{4} + (\tau_{z\theta})^2}. \tag{2}$$

The principal stress orientation angle β was calculated based on Equation (1).

$$\beta = \frac{1}{2} \arctan \frac{2\tau_{z\theta}}{\sigma_z - \sigma_\theta}. \tag{3}$$

The inner and outer pressures were maintained at the same value in all tests, the intermediate principal stress coefficient b can be formulated as follows according to the study by Lade et al. [47].

$$b = \sin \beta^2. \tag{4}$$

Figure 12 shows the change in principal stress and the principal stress orientation during tests. From Table 4, Figure 12, and Equation (2), the maximal principal stress increased and the minimal principal stress decreased as torque was applied. The intermediate principal stress remained constant in the tests. Further, the peak torque showed a slight increase with increases in the cell pressure, which resulted in an increase in β. The 3D reconstruction image of the fracture is shown in Figure 13, where the red, green, and blue arrows stand for X, Y, and Z directions, respectively. The inclination angle, volume, and superficial area of the C-T fractures are documented in Table 5 based on the 3D reconstruction results. In Table 5, δ_{ε_a} and δ_{ε_r} are the axial and lateral strain increments between the torsion application stage and after peak torque stage, respectively. The C-T fracture in Table 5 refers to the largest fracture when multiple-fractures generated in a test.

5.2. C-T Fractures and Discussion. The overlying stratum self-weight of Cretaceous sandstones was about 2.0 MPa considering that a shallowest burial depth of Cretaceous sandstones is less than 100 m in BET as described in Section 3. The maximal cell pressure in the test was thus 2.0 MPa. As seen from Figure 13, there was one fracture under a cell pressure of 0 MPa, two conjugated fractures occurred under a cell pressure of 0.5 MPa, and four conjugated fractures occurred under a cell pressure of 2.0 MPa, indicating that the brittleness of 3DP sandstone tended to decrease with the increase of cell pressure because of the compaction effect from cell pressure. Therefore, a relatively small cell pressure in the test applied on 3DP sandstone might model the C-T fracture formation mechanism within Cretaceous sandstones under a relatively high pressure in shaft sinking sites.

As shown in Table 5, the CT imaged lateral strain of 3DP sandstone exhibited a pronounced increment after peak torque compared with that in the torsion application stage where axial strain remained almost constant. The maximum increment was over 9 times greater than that in the torsion application stage. This was primarily related to C-T fracture formation. Table 5 and Figure 13 show that the C-T fracture fully penetrated the sandstone specimen except under a cell pressure of 0.5 MPa. Moreover, the width of maximum C-T fracture decreased from 2.25 mm to 1.02 mm as the cell pressure increased from 0 MPa to 2.0 MPa. According to Equation (3), the maximal principal stress rotated following a direction similar to torque. Therefore, the maximal principal stress in the specimen was parallel to the fracture and produced an inclination-slip effect in the sandstone along the C-T fracture. While the minimal principal stress was perpendicular to the C-T fracture and had a width-stretching effect on the C-T fracture. The inclination-slip was about 0.1 ± 0.02 mm to 0.2 ± 0.02 mm as shown in Figure 14 and the width-stretching was over 1.0 mm as shown in Table 5. Besides, the volume and superficial area of the C-T fractures tended to decrease as the cell pressure increased as indicated in Table 5. But the change of the volume of the C-T fractures was greater than that of the superficial area.

According to Griffith criteria and Mohr-Coulomb criteria, the tensile stress σ_T and the shear stress τ_n corresponding to shear strength of τ_f in 3DP sandstones after peak torque stage
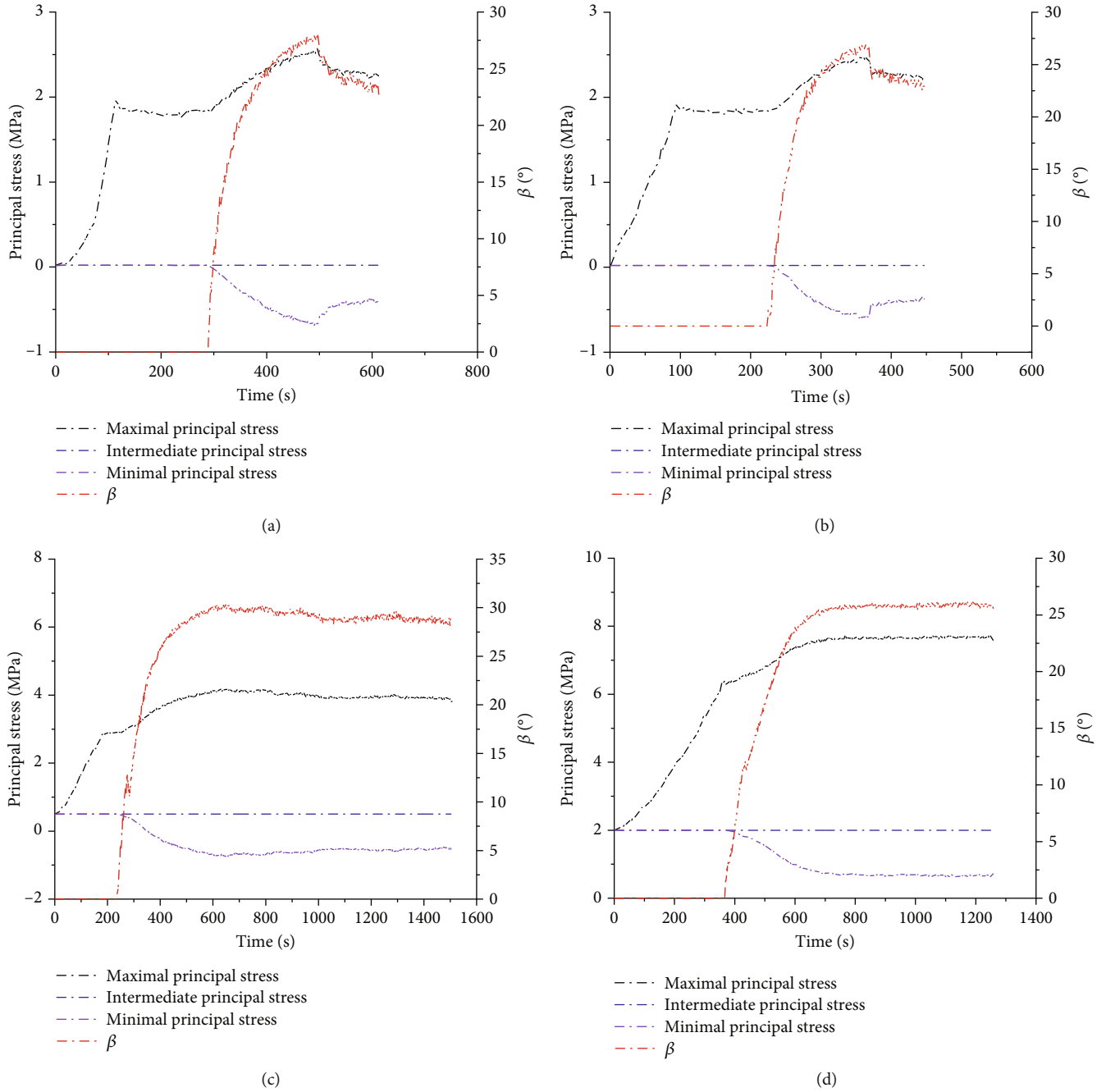
FIGURE 12: Principal stress and its orientation under cell pressures of (a) 0.0 MPa, (b) 0.02 MPa, (c) 0.5 MPa, and (d) 2.0 MPa.

were calculated as follows:

$$\frac{\sigma_T}{\sigma_t} = \frac{(\sigma_1 - \sigma_3)^2}{8(\sigma_1 + \sigma_3)},$$

$$\frac{\tau_n}{\tau_f} = \frac{(\sigma_1 - \sigma_3)\cos\varphi}{2c + [(\sigma_1 + \sigma_3) - (\sigma_1 - \sigma_3)\sin\varphi]\tan\varphi}. \quad (5)$$

Based on the data listed in Tables 3 and 5, the σ_T/σ_t under the four cell pressures were 0.17, 0.47, 0.70, and 0.71, respectively, with an average $\sigma_T/\sigma_t = 0.51$, whereas τ_n/τ_f under var-

ious cell pressures exceeded $\tau_n/\tau_f = 1.0$ except for $\tau_n/\tau_f = 0.45$ under the uniaxial compression. Calculated σ_T/σ_t or τ_n/τ_f values greater than 1.0 implied that the tension or shear fractures occurred. Clearly, the calculated $\tau_n/\tau_f > 1.0$ was greater than the calculated $\sigma_T/\sigma_t < 1.0$. The observed fracture was thus primarily due to shear action. The stretching effect derived from torsion was relatively small even without considering the influence of intermediate principal stress.

As shown in Figure 15, the roughness measurement of 3DP sandstone specimen under a cell pressure of 2.0 MPa indicated that the peak and trough of the fluctuating C-T
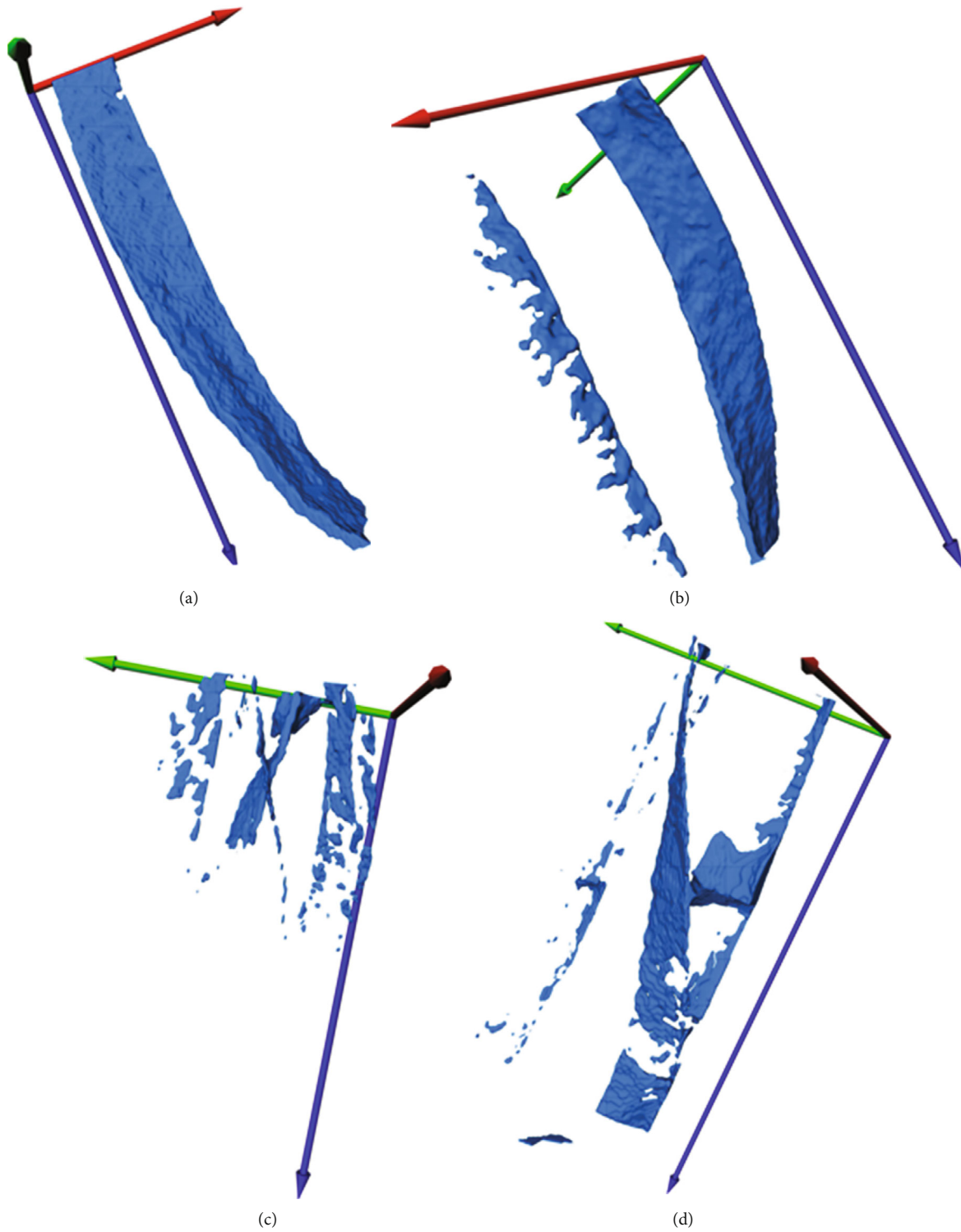
FIGURE 13: C-T fractures under cell pressures of (a) 0.0 MPa, (b) 0.02 MPa, (c) 0.5 MPa, and (d) 2.0 MPa.

fracture surface were 0.592 mm and -0.579 mm, respectively. So the maximal slip induced C-T fracture open perpendicular to fracture inclination was 1.17 mm, which approached the C-T fracture width of 1.02 mm as indicated in Table 5. Therefore, the observed inclination-slip and width-stretching phenom-

ena originated from the shear action and shear-induced slip at the coarse fracture surface, respectively.

Both the inclination angle of C-T fracture ω_{fracture} and the orientation angle of maximal principal stress β slightly increased as the cell pressure increased as indicated by

TABLE 5: Characterization parameters of C-T fractures.

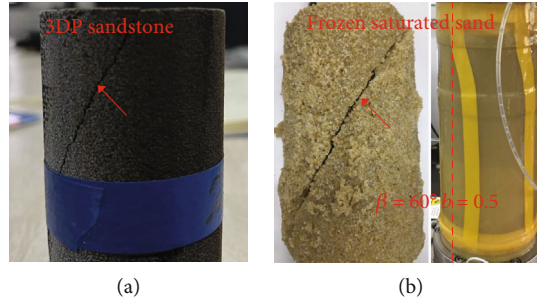|	δ_{ε_a} (%)	δ_{ε_r} (%)	$\sigma_1/\sigma_2/\sigma_3$ (MPa)	b	β (°)	V_{fracture} (mm^3)	S_{fracture} (mm^2)	ω_{fracture} (°)	Fracture width (mm)
#1	0.02	2.23	2.11/0.0/-0.29	0.12	20.3	2471.6	2658.8	22	2.25
#2	0.03	1.45	2.24/0.02/-0.39	0.16	23.3	2129.3	2731.6	23	2.03
#3	0	1.47	3.80/0.5/-0.50	0.23	28.8	—	—	—	1.99
#4	0	1.21	7.59/2.0/0.73	0.19	25.5	1193.9	2401.9	25	1.02

(a)

(b)

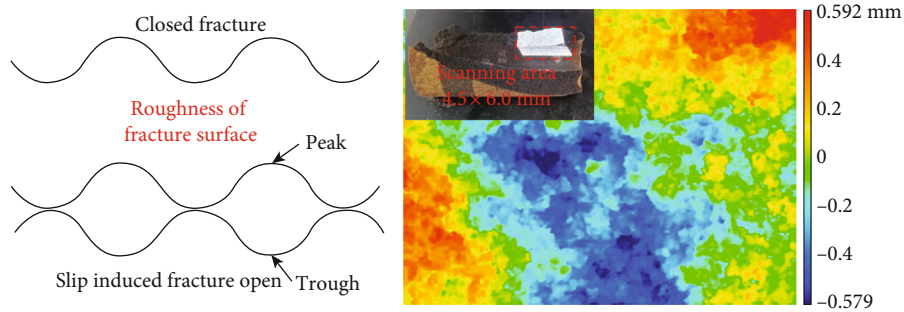FIGURE 14: C-T fractures in (a) 3DP sandstone, and (b) frozen saturated sand (after [44]).

FIGURE 15: Roughness of C-T fracture surface.

Figure 16. Particularly, the inclination angle of the C-T fracture was almost identical to the orientation angle of maximal principal stress. They approached $45° - \varphi/2 = 21.5°$, and were away from the measured orientation of major axes of largest proportion of grains in sandstone specimens with an angle of about 52° to 55°. Obviously, C-T fractures were analogous to the high-angle fractures widely observed by scholars during field investigation [16, 20]. However, the deviation between ω_{fracture} and $45° - \varphi/2 = 21.5°$ tended to increase with the increased cell pressure.

To further interpret of ω_{fracture}, the inclination angles of C-T fracture in frozen saturated sand after tests were gathered and then analyzed [44]. The cementing agent in the frozen saturated sand was pore ice, while it was furan resin in the 3DP sandstones. The brittleness of the cementing agent determined the brittleness of the specimen. So, the measured ω_{fracture} in the frozen saturated sand was greater than that in the 3DP sandstones as illustrated in Table 5, Figures 14 and 17. Further, the measured ω_{fracture} increased as the orientation angle β increased, but it decreased as the intermediate principal stress coefficient b increased as observed in Figure 17. According to
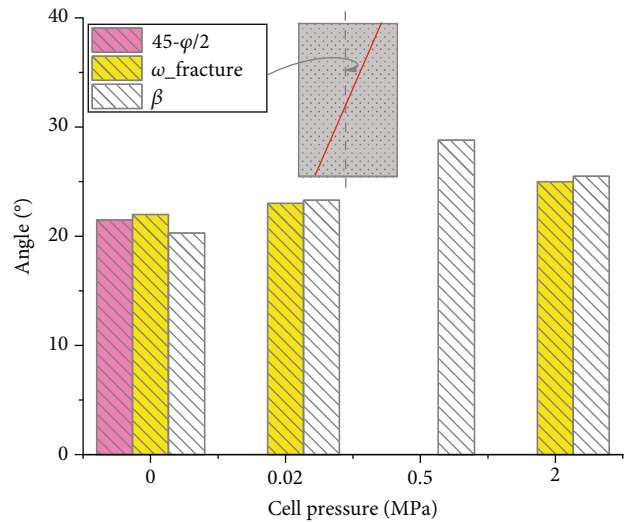
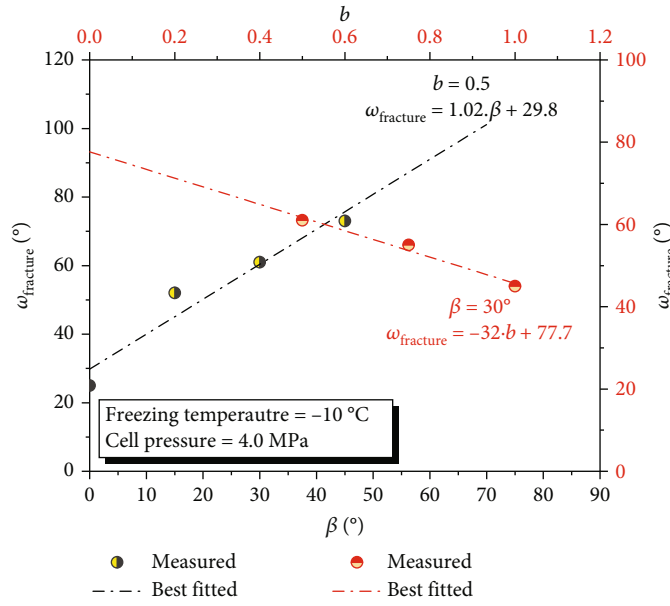FIGURE 16: Comparisons between β and ω_{fracture}.

FIGURE 17: $\omega_{fracture}$ vs. β and b in frozen saturated sand.

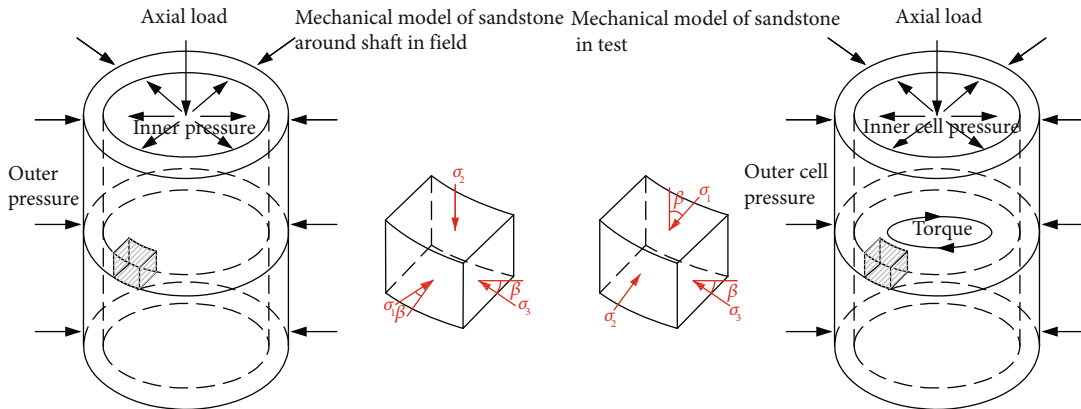FIGURE 18: Mechanical model of sandstone around shaft in field and in laboratory tests.

the linear regression, an increment in the orientation angle β of 5.2° resulted from a cell pressure increase of 2.0 MPa in the 3DP sandstone, which caused an 5.3° increment in the $\omega_{fracture}$. However, the increment of the intermediate principal stress coefficient b was 0.07, which caused a 2.2° decrement in $\omega_{fracture}$. Thus, the net increment of $\omega_{fracture}$ was 3.1°. If the coupling effect between β and b on $\omega_{fracture}$ was not considered, the above-mentioned estimation would accord well with the measured data in Table 5.

As reported by Dang et al. [16], the intermediate principal stress in Ordos basin was almost vertical. Most zones within Ordos basin are flat, so the shafts run perpendicular to the structural convergence plane, but it was oblique of the convergence plane within the orogen-basin transition zone [16, 18, 21]. Convergence was the independent reason for altering the orientation of intermediate principal stress. In general, convergence occurred at a horizontal plane with the maximal principal stress rotating on the horizontal plane. From Figure 18, the

intermediate principal stress in the test was horizontal with the maximal principal stress rotating on the circumferential plane under the torsion action. In other words, the stress state in the test corresponded to the stress state in the field sandstone around the shaft. Hence, the developed X-ray CT-aided C-T apparatus can accurately model stress rotation due to tectonic action around shafts while synchronously visualizing the C-T fracture formation and further the C-T fracture variation arising from shaft sinking and shaft lining maintenance.

6. Conclusions

A real-time X-ray CT-aided C-T apparatus was developed, and a binder jetting-based 3D printing method was used to prepare the unavailable sandstone cores with a weak cementation and high porosity. The C-T fractures in 3DP sandstones were visualized and quantitatively analyzed based on detailed comparisons with field investigations of C-T

fractures in Cretaceous sandstones. The following conclusions were drawn based on this study:

(1) The developed X-ray CT-aided C-T apparatus can accurately model the rotation and variation of the main principal stress derived from tectonic convergence and while simultaneously obtaining real-time C-T fracture

(2) The main physical and mechanical indexes of 3DP sandstones approached the unavailable Cretaceous sandstone cores. Particularly, the 3DP sandstone had obvious specimen-scaled anisotropic properties due to the irregular grains and the unique skeleton structure derived from 3D printing process

(3) A noticeable strain gradient of 2.0 %/mm perpendicular to the C-T fracture in the 3DP sandstone was observed. The average width of the zone characterized by this remarkable strain gradient neighboring the C-T fractures was approximately 2.75 mm, and it was over 1.5 times greater than C-T fracture width

(4) The high inclination angle of C-T fracture measured by X-ray CT was analogous to the reported field observations. The inclination angle of the C-T fracture and the orientation angle of the maximal principal stress were nearly identical, and both increased as the cell pressure increased

(5) The maximal and minimal principal stresses in the 3DP sandstones were approximately parallel and perpendicular to the C-T fractures and thus caused inclination-slip and width-stretching effects to the C-T fracture, respectively, during C-T fracture generation

Data Availability

All data, models, and code generated or used during the study appear in the submitted article.

Conflicts of Interest

The authors declare they have no competing financial interests.

Authors' Contributions

Xiaodong Zhao was assigned in writing, review, and editing. Xu Cai was tasked in original draft. Xingya Zhou, Zejin Lai, and Qingwen Zhong performed the data collection and writing. Zhaoxiang Chu and Guoqing Zhou were tasked in methodology. Hong Li was assigned in investigation.

Acknowledgments

References

[1] J. D. Fan, H. Feng, Z. Y. Song et al., "Key technology and equipment of intelligent mine construction of whole mine mechanical rock breaking in Kekegai coal mine," *Journal of China Coal Society*, vol. 47, no. 1, pp. 499–514, 2022, (in Chinese).

[2] C. B. Basnet and K. K. Panthi, "Analysis of unlined pressure shafts and tunnels of selected Norwegian hydropower projects," *Journal of Rock Mechanics and Geotechnical Engineering*, vol. 10, no. 3, pp. 486–512, 2018.

[3] W. P. Li and X. Q. Li, "Mechanism of rupture of shaft linings in coal mine areas buried by thick over-soils in East China," *Geotechnique*, vol. 55, no. 3, pp. 237–244, 2005.

[4] X. D. Zhao, G. Q. Zhou, G. S. Zhao, and X. C. Hu, "Fracture controlling of vertical shaft lining using grouting into neighboring soil deposits: a case study," *Soils and Foundations*, vol. 57, no. 5, pp. 882–891, 2017.

[5] B. Liu, Y. J. Ma, G. Zhang, and W. Xu, "Acoustic emission investigation of hydraulic and mechanical characteristics of muddy sandstone experienced one freeze-thaw cycle," *Cold Regions Science and Technology*, vol. 151, pp. 335–344, 2018.

[6] Q. Liu, Y. J. Sun, and J. Li, "Experimental study on seepage characteristics of Jurassic weakly cemented sandstone under water-rock interaction," *Geofluids*, vol. 2020, article 8543687, 12 pages, 2020.

[7] L. D. Meng, L. J. Han, Q. B. Meng, K. X. Liu, M. L. Tian, and H. X. Zhu, "Study on characteristic and energy of argillaceous weakly cemented rock under dynamic loading by Hopkinson bar experiment," *Energies*, vol. 13, no. 12, p. 3215, 2020.

[8] Z. Y. Song, H. G. Ji, Z. Q. Liu, and L. H. Sun, "Study on the critical stress threshold of weakly cemented sandstone damage based on the renormalization group method," *International Journal of Coal Science & Technology*, vol. 7, no. 4, pp. 693–703, 2020.

[9] J. H. Han, J. Q. Zou, W. H. Yang, and C. C. Hu, "Mechanism of fracturing in shaft lining caused by high-pressure pore water in stable rock strata," *Mathematical Problems in Engineering*, vol. 2019, article 5234642, Article ID 5234642, 9 pages, 2019.

[10] Y. Bai, R. L. Shan, Y. Ju, Y. X. Wu, P. F. Sun, and Z. E. Wang, "Study on the mechanical properties and damage constitutive model of frozen weakly cemented red sandstone," *Cold Regions Science and Technology*, vol. 171, article 102980, 2020.

[11] B. Liu, Y. D. Sun, B. Wang, Y. H. Han, R. H. Zhang, and J. X. Wang, "Effect of water content on mechanical and electrical characteristics of the water-rich sandstone during freezing," *Environmental Earth Sciences*, vol. 79, no. 10, p. 236, 2020.

[12] W. D. Zhang, Z. C. Yang, and Y. M. Wei, "Advances in research of hydraulic fractures in unconsolidated sands," *Mechanics in Engineering*, vol. 36, no. 4, pp. 396–402, 2014, (in Chinese).

[13] Z. H. Zhao, H. Liu, X. Z. Lyu, L. Wang, Z. X. Tian, and J. C. Sun, "Experimental study on the damage and deterioration behaviour of deep soft rock under water-rock interaction," *Geofluids*, vol. 2021, article 8811110, Article ID 8811110, 11 pages, 2021.

[14] G. W. Fan, M. W. Chen, D. S. Zhang et al., "Experimental study on the permeability of weakly cemented rock under different stress states in triaxial compression tests," *Geofluids*, vol. 2018, article 9035654, p. 9, 2018.

[15] G. X. Cheng, B. Jiang, M. Li, F. L. Li, and M. Zhu, "Structural evolution of southern Sichuan Basin (South China) and its control effects on tectonic fracture distribution in Longmaxi shale," *Journal of Structural Geology*, vol. 153, article 104465, 2021.

[16] B. Dang, H. Zhao, M. M. Qu et al., "Distribution characteristics, genesis analyses, and research significance of Triassic regional structural fractures in the Ordos Basin, Central China," *Geological Journal*, vol. 53, no. S1, pp. 212–224, 2018.

[17] J. M. Fan, X. F. Qu, C. Wang, Q. H. Lei, L. B. Cheng, and Z. Q. Yang, "Natural fracture distribution and a new method predicting effective fractures in tight oil reservoirs in Ordos Basin, NW China," *Petroleum Exploration and Development*, vol. 43, no. 5, pp. 806–814, 2016.

[18] P. Guo, D. S. Ren, and Y. H. Xue, "Simulation of multi-period tectonic stress fields and distribution prediction of tectonic fractures in tight gas reservoirs: a case study of the Tianhuan depression in western Ordos Basin, China," *Marine and Petroleum Geology*, vol. 109, pp. 530–546, 2019.

[19] J. B. Peng, L. W. Chen, Q. B. Huang, Y. M. Men, W. Fan, and J. K. Yan, "Physical simulation of ground fissures triggered by underground fault activity," *Engineering Geology*, vol. 155, pp. 19–30, 2013.

[20] L. B. Zeng, W. Y. Lyu, J. Li et al., "Natural fractures and their influence on shale gas enrichment in Sichuan Basin, China," *Journal of Natural Gas Science and Engineering*, vol. 30, pp. 1–9, 2016.

[21] J. C. Zhang, H. R. Zheng, G. L. Wang et al., "In-situ stresses, abnormal pore pressures and their impacts on the Triassic Xujiahe reservoirs in tectonically active western Sichuan basin," *Marine and Petroleum Geology*, vol. 122, article 104708, 2020.

[22] I. Baroň, L. Sokol, R. Melicharc, and L. Plan, "Gravitational and tectonic stress states within a deep-seated gravitational slope deformation near the seismogenic periadriatic line fault," *Engineering Geology*, vol. 261, article 105284, 2019.

[23] J. O. Eisermann, P. L. Göllner, and U. Riller, "Orogen-scale transpression accounts for GPS velocities and kinematic partitioning in the southern Andes," *Communications Earth & Environment*, vol. 2, no. 1, article 167, 2021.

[24] J. S. Yu, K. Tan, C. H. Zhang, B. Zhao, D. Z. Wang, and Q. Li, "Present-day crustal movement of the Chinese mainland based on global navigation satellite system data from 1998 to 2018," *Advances in Space Research*, vol. 63, no. 2, pp. 840–856, 2019.

[25] Q. Yan, B. Li, Y. Zhang, and C. He, "In situ automatic monitoring and working state assessment of inclined shafts in coal mines," *Proceedings of the Institution of Civil Engineers: Geotechnical Engineering*, vol. 174, no. 4, pp. 390–405, 2021.

[26] N. Watanab, T. Ishibashi, Y. Ohsaki et al., "X-ray CT based numerical analysis of fracture flow for core samples under various confining pressures," *Engineering Geology*, vol. 123, no. 4, pp. 338–346, 2011.

[27] H. Y. Zhuang, R. Wang, G. X. Chen, Y. Miao, and K. Zhao, "Shear modulus reduction of saturated sand under large liquefaction-induced deformation in cyclic torsional shear tests," *Engineering Geology*, vol. 240, no. 5, pp. 110–122, 2018.

[28] D. Chen, D. Y. Wang, W. Ma, L. L. Lei, and G. Y. Li, "A strength criterion for frozen clay considering the influence of stress lode angle," *Canadian Geotechnical Journal*, vol. 56, no. 11, pp. 1557–1572, 2019.

[29] Y. Wang, T. Q. Mao, Y. J. Xia, X. Li, and X. F. Yi, "Macro-meso fatigue failure of bimrocks with various block content subjected to multistage fatigue triaxial loads," *International Journal of Fatigue*, vol. 163, article 107014, 2022.

[30] Y. Wang, P. F. Tan, J. Q. Han, and P. Li, "Energy-driven fracture and instability of deeply buried rock under triaxial alternative fatigue loads and multistage unloading conditions: prior fatigue damage effect," *International Journal of Fatigue*, vol. 168, article 107410, 2023.

[31] K. Ueta, K. Tani, and T. Kato, "Computerized X-ray tomography analysis of three-dimensional fault geometries in basement-induced wrench faulting," *Engineering Geology*, vol. 56, no. 1-2, pp. 197–210, 2000.

[32] Y. Wang, X. F. Yi, P. Li, M. F. Cai, and T. Sun, "Macro-meso damage cracking and volumetric dilatancy of fault block-in-matrix rocks induced by freeze–thaw-multistage constant amplitude cyclic (F-T-MSCAC) loads," *Fatigue & Fracture of Engineering Materials & Structures*, vol. 45, no. 10, pp. 2990–3008, 2022.

[33] X. D. Zhao, Y. Wu, Z. J. Lai, and G. Q. Zhou, "A field condition-based test method for artificially frozen soils," *Géotechnique Letters*, vol. 9, no. 1, pp. 1–7, 2019.

[34] Y. H. Li, P. Wu, W. G. Liu, X. Sun, Z. Cui, and Y. C. Song, "A microfocus X-ray computed tomography based gas hydrate triaxial testing apparatus," *Review of Scientific Instruments*, vol. 90, no. 5, article 055106, 2019.

[35] X. D. Zhao, Z. Y. Lv, Y. Zhou, Z. X. Chu, Y. K. Ji, and X. Y. Zhou, "Thermal and pore pressure gradient–dependent deformation and fracture behavior of saturated soils subjected to freeze-thaw," *Bulletin of Engineering Geology and the Environment*, vol. 81, no. 5, article 188, 2022.

[36] C. Jiang and G. F. Zhao, "A preliminary study of 3D printing on rock mechanics," *Rock Mechanics and Rock Engineering*, vol. 48, no. 3, pp. 1041–1050, 2015.

[37] D. Vogler, S. D. C. Walsh, E. Dombrovski, and M. A. Perras, "A comparison of tensile failure in 3D-printed and natural sandstone," *Engineering Geology*, vol. 226, pp. 221–235, 2017.

[38] Y. J. Xia, C. Q. Zhang, H. Zhou et al., "Mechanical behavior of structurally reconstructed irregular columnar jointed rock mass using 3D printing," *Engineering Geology*, vol. 268, article 105509, 2020.

[39] J. B. Zhu, T. Zhou, Z. Y. Liao, L. Sun, X. B. Li, and R. Chen, "Replication of internal defects and investigation of mechanical and fracture behaviour of rock using 3D printing and 3D numerical methods in combination with X-ray computerized tomography," *International Journal of Rock Mechanics and Mining Sciences*, vol. 106, pp. 198–212, 2018.

[40] G. C. Hou, M. S. Zhang, and F. Liu, *Exploration Study of Underground Water in Ordos Basin*, Geology Press, Beijing, 2008, (in Chinese).

[41] H. G. Li, H. M. Li, H. J. Wang, and S. L. Chen, "Physical and mechanical characteristics and definition of weakly cemented sandstone," *Coal Science and Technology*, vol. 45, pp. 1–7, 2017, (in Chinese).

[42] H. M. Li, H. G. Li, S. S. Peng, F. Du, and Y. F. Liang, *Physical and Mechanical Properties of Rock in Shendong Mine Area*, Science Press, Beijing, 2018, (in Chinese).

[43] R. Altindag, "The evaluation of rock brittleness concept on rotary blast hole drills," *Journal Of The South African Institute Of Mining & Metallurgy*, vol. 102, no. 1, pp. 61–66, 2002.

[44] Z. J. Lai, *Experimental Study on Mechanical Properties of Frozen Saturated Medium Sand in Directional Shear Path, [Ph.D. thesis]*, China University of Mining and Technology, Xuzhou, China, 2021, (in Chinese).

[45] P. T. Yeh, K. Z. Lee, and K. T. Chang, "3D effects of permeability and strength anisotropy on the stability of weakly cemented rock slopes subjected to rainfall infiltration," *Engineering Geology*, vol. 266, article 105459, 2020.

[46] S. W. Hao, H. Y. Wang, M. F. Xia, F. J. Ke, and Y. L. Bai, "Relationship between strain localization and catastrophic rupture," *Theoretical and Applied Fracture Mechanics*, vol. 48, no. 1, pp. 41–49, 2007.

[47] P. V. Lade, J. Nam, and W. P. Hong, "Shear banding and cross-anisotropic behavior observed in laboratory sand tests with stress rotation," *Canadian Geotechnical Journal*, vol. 45, no. 1, pp. 74–84, 2008.